

# Adsorption of Sulfur Dioxide in Cu(II)-Carboxylate Framework Materials: The Role of Ligand Functionalization and Open Metal Sites

Weiyao Li,<sup>#</sup> Jiangnan Li,<sup>#</sup> Thien D. Duong,<sup>#</sup> Sergei A. Sapchenko, Xue Han, Jack D. Humby, George F. S. Whitehead, Iñigo J. Victórica-Yrezábal, Ivan da Silva, Pascal Manuel, Mark D. Frogley, Gianfelice Cinque, Martin Schröder,<sup>\*</sup> and Sihai Yang<sup>\*</sup>

Cite This: *J. Am. Chem. Soc.* 2022, 144, 13196–13204

Read Online

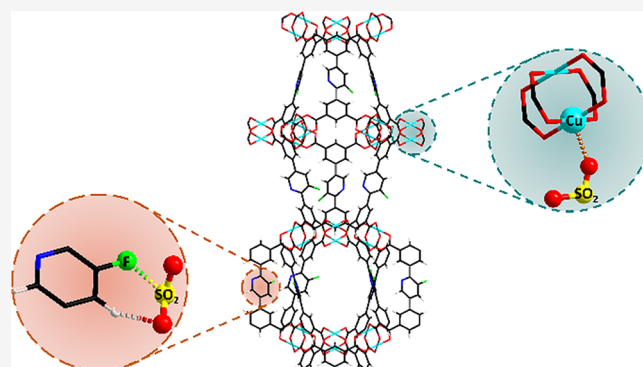
ACCESS |

Metrics & More

Article Recommendations

Supporting Information

**ABSTRACT:** The development of efficient sorbent materials for sulfur dioxide (SO<sub>2</sub>) is of key industrial interest. However, due to the corrosive nature of SO<sub>2</sub>, conventional porous materials often exhibit poor reversibility and limited uptake toward SO<sub>2</sub> sorption. Here, we report high adsorption of SO<sub>2</sub> in a series of Cu(II)-carboxylate-based metal–organic framework materials. We describe the impact of ligand functionalization and open metal sites on the uptake and reversibility of SO<sub>2</sub> adsorption. Specifically, MFM-101 and MFM-190(F) show fully reversible SO<sub>2</sub> adsorption with remarkable capacities of 18.7 and 18.3 mmol g<sup>-1</sup>, respectively, at 298 K and 1 bar; the former represents the highest reversible uptake of SO<sub>2</sub> under ambient conditions among all porous solids reported to date. *In situ* neutron powder diffraction and synchrotron infrared microspectroscopy enable the direct visualization of binding domains of adsorbed SO<sub>2</sub> molecules as well as host–guest binding dynamics. We have found that the combination of open Cu(II) sites and ligand functionalization, together with the size and geometry of metal–ligand cages, plays an integral role in the enhancement of SO<sub>2</sub> binding.



## INTRODUCTION

Fossil fuels will continue to dominate the energy landscape in the decades to come, leading to significant emissions of SO<sub>2</sub>.<sup>1</sup> Air pollution by SO<sub>2</sub> has detrimental effects on both human health and the environment,<sup>2–5</sup> and SO<sub>2</sub> in the atmosphere is thus a major source of pollution and is associated with global climate change.<sup>3,4</sup> SO<sub>2</sub> is also an important industrial feedstock primarily for the manufacture of sulfuric acid, which uses 98% of the total production of SO<sub>2</sub>.<sup>6</sup> Although the state-of-the-art flue-gas desulfurization (FGD) technologies can remove up to 95% SO<sub>2</sub>, they generate a tremendous amount of solid waste, and residual SO<sub>2</sub> can later poison CO<sub>2</sub> scrubbers downstream of FGD processes.<sup>7</sup> Regenerable methods can mitigate the production of waste by recycling the sorbent post SO<sub>2</sub> adsorption, and the recovered SO<sub>2</sub> can be used further for the synthesis of sulfuric acid. Sorbent materials with high SO<sub>2</sub> capacity can be used as a safe host for the transport of SO<sub>2</sub>, eliminating the energy cost for its reduction to elemental sulfur followed by re-oxidation to SO<sub>2</sub>.<sup>6</sup> Traditional porous materials including metal oxides,<sup>8</sup> activated carbons,<sup>9</sup> and zeolites<sup>10</sup> have been tested for SO<sub>2</sub> adsorption. However, these materials tend to demonstrate low SO<sub>2</sub> capacities under ambient conditions

(usually in the range of 1–5 mmol g<sup>-1</sup>) owing to their limited surface areas and often they undergo irreversible structural degradation upon the harsh conditions required to remove adsorbed or bound SO<sub>2</sub>.<sup>11</sup>

Metal–organic frameworks (MOFs) are promising sorbent materials owing to their exceptional surface area and tuneable pore environments.<sup>12,13</sup> Functionalization of the organic linker and/or incorporation of coordinatively unsaturated metal sites can deliver targeted properties to the resultant MOFs, such as preferential adsorption of H<sub>2</sub>, CH<sub>4</sub>, CO<sub>2</sub>, and light hydrocarbons.<sup>14–18</sup> The use of MOF materials as SO<sub>2</sub> sorbents is currently a rapidly developing field of study.<sup>19–32</sup> MOF-177 exhibits a record high SO<sub>2</sub> uptake of 25.7 mmol g<sup>-1</sup> at 298 K and 1 bar, but it shows irreversible structural degradation upon desorption.<sup>22</sup> Considering that over 100,000 MOFs are

Received: March 27, 2022

Published: July 18, 2022



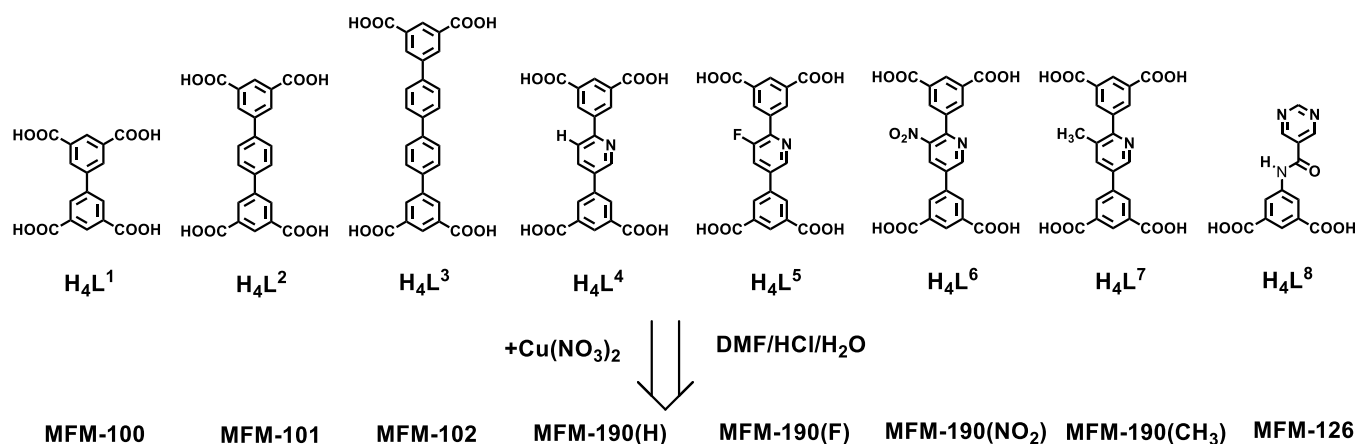


Figure 1. Structures of  $H_4L^1$ – $H_4L^8$  and nomenclature for their corresponding Cu(II)-based MOFs.

reported to date,<sup>33</sup> samples that are stable to repeated exposure to  $SO_2$  are still relatively rare, including MFM-300(In) (8.28  $mmol\ g^{-1}$ ),<sup>23</sup> MFM-300(Sc) (9.4  $mmol\ g^{-1}$ ),<sup>24</sup> DMOF (9.97  $mmol\ g^{-1}$ ),<sup>25</sup> NU-1000 (10.9  $mmol\ g^{-1}$ ),<sup>26</sup> SIFSIX-1-Cu (11.0  $mmol\ g^{-1}$ ),<sup>27</sup> NU-200 (11.7  $mmol\ g^{-1}$ ),<sup>28</sup> MFM-601 (12.3  $mmol\ g^{-1}$ ),<sup>29</sup> MFM-300(Sc)@EtOH (13.2  $mmol\ g^{-1}$ ),<sup>24</sup> MOF-808 (15.3  $mmol\ g^{-1}$ ),<sup>30</sup> MFM-170 (17.5  $mmol\ g^{-1}$ ),<sup>31</sup> and MIL-101(Cr)-4F(1%) (18.4  $mmol\ g^{-1}$ )<sup>32</sup> (uptake given at 298 K and 1 bar of  $SO_2$ ). Systems incorporating open metal sites that are capable of capturing  $SO_2$  are extremely rare.<sup>31</sup> Thus, the optimization of pore environment in terms of ligand functionalization, implementation of open metal sites, and control of pore geometry is an important approach to achieve reversible, high adsorption of  $SO_2$ .

Here, we report a comprehensive investigation of adsorption of  $SO_2$  in a series of Cu(II)-carboxylate-based MOFs, namely, MFM-100, MFM-101, MFM-102, MFM-126, MFM-190(F), MFM-190( $NO_2$ ), MFM-190( $CH_3$ ), and MFM-190(H) (published previously as ZJU-5), showing metal–ligand cages of different sizes and showing combinations of open Cu(II) sites and functional groups within the cages. MFM-126 has a (3,6)-connected framework with an *eea* topology with  $[Cu_2(OOCR)_4]$  paddlewheels bound to carboxylate and pyrimidyl groups of the linker in the equatorial and axial positions, respectively, leaving no open Cu(II) sites. The other materials in this series crystallize in *nbo* topology with  $[Cu_2(OOCR)_4]$  paddlewheels bound to carboxylate donors of the linker and water molecules at the equatorial and axial positions, respectively. Open Cu(II) sites can be generated by removal of the terminally bound water molecules by heating under vacuum. MFM-101 and MFM-190(F), the latter with a fluoro-functionalization, show fully reversible adsorption of  $SO_2$  of 18.7 and 18.3  $mmol\ g^{-1}$  at 298 K and 1 bar, respectively; the former represents the highest reversible uptake of  $SO_2$  in porous solids. These two materials also show high stability toward cyclic adsorption and desorption of  $SO_2$ , retaining full crystallinity and uptake capacity over multiple cycles. The other systems show a decrease in uptake, porosity, or crystallinity upon repeated cycles of adsorption–desorption. The host–guest binding interaction and locations of adsorbed  $SO_2$  molecules in MFM-190(F) and MFM-126 have been visualized by *in situ* neutron powder diffraction (NPD), inelastic neutron scattering (INS), and synchrotron infrared microspectroscopy studies. These reveal that a combination of open Cu(II) sites and ligand functionalization,

along with the size and geometry of metal–ligand cages, results in the exceptional adsorption of  $SO_2$  in MFM-190(F).

## RESULTS AND DISCUSSION

**Synthesis and Structural Analysis.** Three new MOFs, namely, MFM-190(F), MFM-190( $NO_2$ ), and MFM-190( $CH_3$ ), along with previously reported<sup>34–36</sup> MFM-100, MFM-101, MFM-102, MFM-190(H), and MFM-126, were synthesized *via* solvothermal reactions of carboxylate ligands and  $Cu(NO_3)_2$  in dimethylformamide (DMF) (Figure 1). Powder X-ray diffraction (PXRD) confirmed the phase purity of all bulk samples (Figures S1–S4). The PXRD patterns confirm that MFM-190(F), MFM-190( $NO_2$ ), and MFM-190( $CH_3$ ) are iso-structural to MFM-190(H) and MFM-101 (Figures S5 and S6). Single-crystal X-ray diffraction shows that MFM-190(F), MFM-190( $NO_2$ ), and MFM-190( $CH_3$ ) crystallize in the trigonal space group *R-3m* and shows *nbo* network topology. The asymmetric unit contains one Cu(II) ion, one quarter of a tetracarboxylate linker, and one terminal water molecule, and the structure is formed by bridging  $[Cu_2(OOCR)_4]$  paddlewheels incorporating di-isophthalate linkers. The resulting framework is composed of two different types of cages in a 1:1 ratio. A cylindrical cage A is constructed by 12  $[Cu_2(OOCR)_4]$  paddlewheels and six linkers with a length of *ca.* 24 Å and width of 18 Å at the equatorial ring. A spherical cage B is made up of six  $[Cu_2(OOCR)_4]$  paddlewheels and six linkers with a diameter of *ca.* 11 Å (Figure 2a). These cages are decorated with  $-H$ ,  $-F$ ,  $-NO_2$ , and  $-CH_3$  groups in MFM-190(H), MFM-190(F), MFM-190( $NO_2$ ), and MFM-190( $CH_3$ ), respectively, as well as pyridyl N centers. These four MOFs have similar thermal stability up to  $\sim 300$  °C (Figure S7)<sup>34</sup> and are iso-reticular to MFM-100, MFM-101, and MFM-102,<sup>35</sup> which also adopt an *nbo* network topology. The linkers of MFM-100, MFM-101, and MFM-102 increase in length along the series with the cage A increasing in length from 14 Å in MFM-100 to *ca.* 33 Å in MFM-102 and cage B increasing in length from 6 Å in MFM-100 to *ca.* 15 Å in MFM-102 as the linker elongates (Figure 2b). MFM-126 crystallizes in the trigonal space group *R-3* and adopts a (3,6)-connected framework with an *eea* network topology. Similar to the *nbo*-type MOFs, MFM-126 is made up of two types of cages, a cylindrical cage A made up of 12  $[Cu_2(OOCR)_4]$  paddlewheels and six linkers with a length of *ca.* 15 Å and a spherical cage B made up of six  $[Cu_2(OOCR)_4]$  paddlewheels and six linkers with a diameter of *ca.* 12 Å.

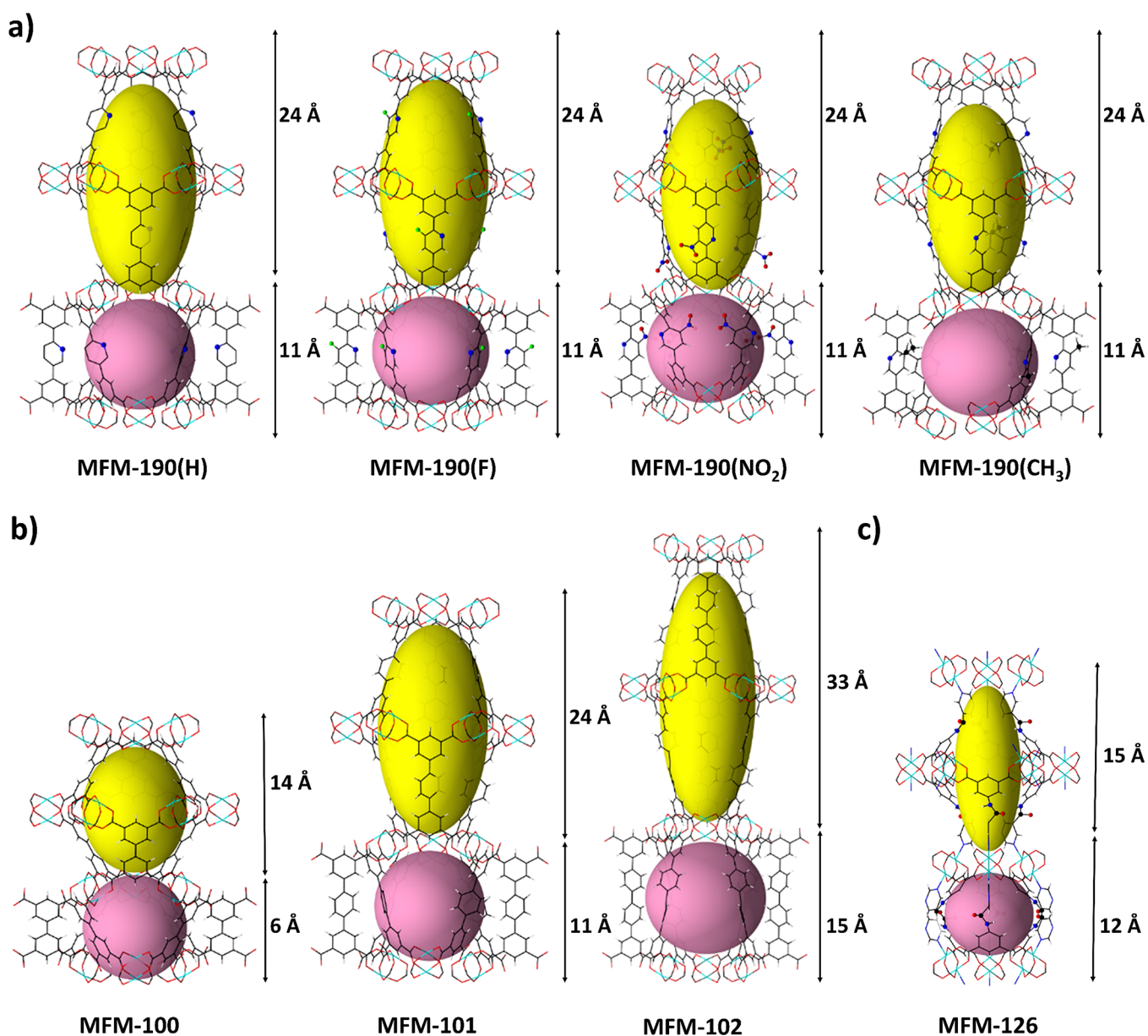


**Figure 2.** Views of the metal–organic cages in the MOFs in this study. Views of (a) MFM-190(H), MFM-190(F), MFM-190(NO<sub>2</sub>), and MFM-190(CH<sub>3</sub>) and (b) MFM-100, MFM-101, and MFM-102, which adopt the *nbo* network topology with open metal sites. (c) View of MFM-126, which adopts the *eea* network topology with no open metal sites. Cu, cyan; C, black; O, red; H, white; N, blue; F, green. Void spaces are highlighted in yellow (cage A) and pink (cage B); the given lengths refer to the sizes of the cages.

However, the axial positions of the [Cu<sub>2</sub>(OOCR)<sub>4</sub>] paddlewheels are capped by pyrimidyl nitrogen centers of the linker, and therefore, no open Cu(II) metal sites are generated upon activation of MFM-126 (Figure 2c).

**Analysis of Gas Adsorption Isotherms and Dynamic Separation of SO<sub>2</sub>.** The BET surface areas of desolvated MFM-100, MFM-101, MFM-102, MFM-126, MFM-190(F), MFM-190(NO<sub>2</sub>), MFM-190(CH<sub>3</sub>), and MFM-190(H) were determined by N<sub>2</sub> adsorption isotherms at 77 K to be 1445, 2300, 2873, 965, 2538, 2304, 2550, and 2373 m<sup>2</sup> g<sup>-1</sup>, respectively. The increase in BET surface area from MFM-100 to MFM-102 is due to the expansion of metal–organic cages as a result of the elongation of the ligands, while ligand functionalization appears to have a limited impact on the BET surface areas of MFM-190(F), MFM-190(NO<sub>2</sub>), MFM-190(CH<sub>3</sub>), and MFM-190(H) (Figure S8).

The gravimetric adsorption isotherms of SO<sub>2</sub> have been recorded for all eight MOFs at 273 and 298 K and from 0 to 1 bar (Figures S11–S18). MFM-101 shows a SO<sub>2</sub> uptake of 20.8 mmol g<sup>-1</sup> (or 1.33 g g<sup>-1</sup>) at 273 K and 1.0 bar, exceeding those reported for all leading sorbent materials for SO<sub>2</sub> under the same conditions, such as MFM-170 (19.4 mmol g<sup>-1</sup>),<sup>31</sup> MFM-601 (16.9 mmol g<sup>-1</sup>),<sup>29</sup> and MFM-202a (12.8 mmol g<sup>-1</sup>).<sup>37</sup> At 298 K and 1 bar, MFM-100, MFM-101, MFM-102, MFM-126, MFM-190(F), MFM-190(NO<sub>2</sub>), MFM-190(CH<sub>3</sub>), and MFM-190(H) show SO<sub>2</sub> uptakes of 7.6, 18.7, 12.1, 7.33, 18.3, 12.7, 15.9, and 14.0 mmol g<sup>-1</sup>, respectively (Figure 3a). Multiple cycles of adsorption–desorption have been tested for all samples at 298 K to identify the reversibility and stability of adsorption. MFM-190(H) displays a loss of 38% in the uptake capacity of SO<sub>2</sub> at 1 bar over six cycles (Figure 3d,e), which is accompanied by a decrease in the BET surface area from 2373

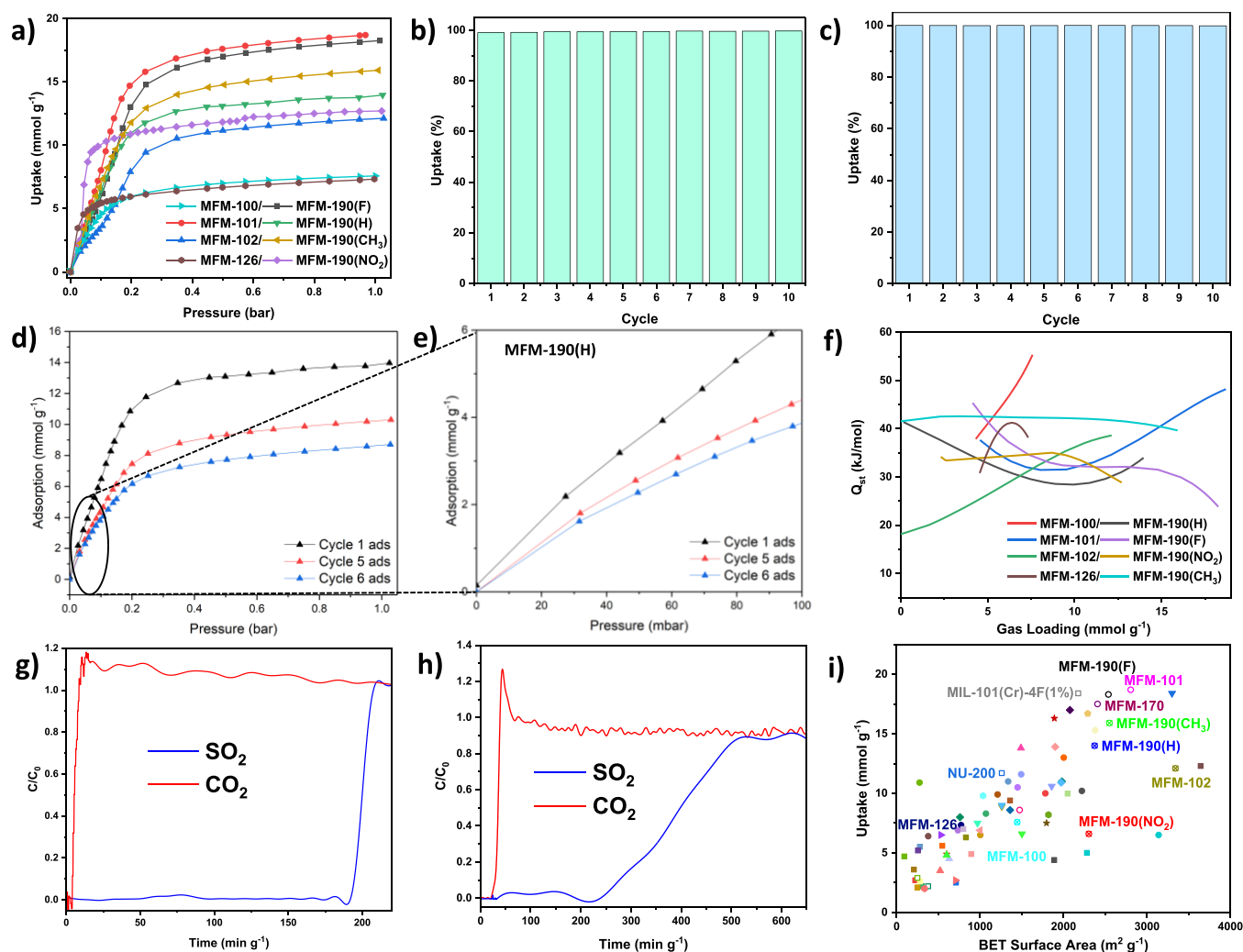


**Figure 3.** (a)  $\text{SO}_2$  adsorption isotherms at 298 K and 1 bar for all materials in this study (desorption isotherms are omitted for clarity and shown in the SI). Cycling of  $\text{SO}_2$  between 0 and 500 mbar at 298 K in (b) MFM-190(F) and (c) MFM-101. (d) Comparison of adsorption of  $\text{SO}_2$  at 298 K for MFM-190(H) over different cycles at 1 bar. (e) View of adsorption of  $\text{SO}_2$  at 298 K for MFM-190(H) over different cycles at 100 mbar. (f) Values for  $Q_{st}$  for  $\text{SO}_2$  in all materials in this study. Breakthrough plots for mixtures of  $\text{SO}_2/\text{CO}_2$  ( $\text{SO}_2/\text{CO}_2$ : 2500 ppm/15%; total flow rate: 30 mL  $\text{min}^{-1}$ ) over a fixed-bed packed at 298 K with (g) MFM-190(F) and (h) MFM-101. (i) Plot of the BET surface area against the  $\text{SO}_2$  adsorption at 1 bar and 298 K for selected MOF materials that show reversible adsorption of  $\text{SO}_2$  (full details are given in Table S3).

to 1959  $\text{m}^2 \text{g}^{-1}$  (Figure S9). The relatively small decrease in porosity (17%) compared with that in  $\text{SO}_2$  uptake (38%) suggests a loss of active sites and porosity due to pore collapse. Analysis of the pore size distribution (PSD) suggests that the pores of pristine MFM-190(H) are centered at around 5 Å and 7–9 Å (Figure S9b), while post- $\text{SO}_2$  exposure, multiple irregular pores are generated with diverse diameters between 15–18 Å and 25–35 Å.

Incorporation of  $-\text{F}$ ,  $-\text{NO}_2$ , and  $-\text{CH}_3$  functionalization has varying impacts on  $\text{SO}_2$  adsorption with uptakes of 18.3, 12.7, and 15.9  $\text{mmol g}^{-1}$  recorded at 298 K and 1 bar in MFM-190(F), MFM-190( $\text{NO}_2$ ), and MFM-190( $\text{CH}_3$ ), respectively, compared with the 14.0  $\text{mmol g}^{-1}$  for the parent MFM-190(H) (Figure 3a). While showing steep adsorption at a low pressure (10.3  $\text{mmol g}^{-1}$  at 0.1 bar), MFM-190( $\text{NO}_2$ ) suffers severe framework collapse upon desorption; the sample post several cycles of adsorption–desorption of  $\text{SO}_2$  shows a marked reduction of the BET surface area from 2304 to 1172  $\text{m}^2 \text{g}^{-1}$  (Figure S10). In contrast, MFM-190(F) and MFM-190( $\text{CH}_3$ ) both show consistent adsorption capacity of  $\text{SO}_2$

over 10 cycles (Figure 3b and Figure S17). However, the comparison of PXRD gives distinct results: while MFM-190( $\text{CH}_3$ ) largely loses its crystallinity post- $\text{SO}_2$  exposure, MFM-190(F) fully retains its crystallinity (Figure S19f,h). Thus, the introduction of  $-\text{F}$  groups to the linker has greatly enhanced the framework stability of MFM-190(F).

MFM-100, MFM-101, and MFM-102 exhibit excess  $\text{SO}_2$  adsorption capacities of 7.6, 18.7, and 12.1  $\text{mmol g}^{-1}$  at 298 K and 1 bar (Figure 3a). A 3.7% loss in uptake capacity over 10 cycles of  $\text{SO}_2$  adsorption at 298 K is observed in MFM-100 (Figure S11b) with the post- $\text{SO}_2$  exposure sample showing broadening and loss of Bragg peaks by PXRD due to reduction in crystallinity and structural order of the sample (Figure S19a). However, MFM-101 shows fully reversible  $\text{SO}_2$  uptake over 10 cycles without any loss in total uptake capacity (Figure 3c). Indeed, comparison of the PXRD pattern for the as-synthesized and post- $\text{SO}_2$  cycling sample of MFM-101 confirmed little change in crystallinity (Figure S19b). Interestingly, although MFM-102 only shows a 5.6% loss in uptake capacity over 10 cycles of  $\text{SO}_2$  adsorption at 298 K

(Figure S13b), comparison of the PXRD patterns of the fresh and post-SO<sub>2</sub> exposure MFM-102 samples shows that there is a significant loss in long-range structural order in the latter (Figure S19c).

MFM-126 displays an excess SO<sub>2</sub> adsorption capacity of 7.3 mmol g<sup>-1</sup> at 298 K and 1 bar (Figure 3a) and shows stable performance over 10 cycles of adsorption–desorption of SO<sub>2</sub> with full reversibility (Figure S14b). This is also evidenced by the PXRD pattern of the post-SO<sub>2</sub> sample of MFM-126, which fully retains its crystallinity (Figure S19d). However, compared with other MOFs, MFM-126 shows a much lower uptake capacity of SO<sub>2</sub>, reflecting potentially the lack of open metal sites.

The ability to capture SO<sub>2</sub> at low concentrations by MFM-190(F) and MFM-101 was tested by dynamic breakthrough experiments with SO<sub>2</sub>-containing gas mixtures at 298 K and 1 bar. Both MFM-190(F) and MFM-101 display excellent dynamic adsorption of SO<sub>2</sub> at a low concentration (2500 ppm SO<sub>2</sub>) (Figures S20 and S21). In addition, MFM-190(F) and MFM-101 successfully capture SO<sub>2</sub> from a mixture of 15% CO<sub>2</sub> and 2500 ppm SO<sub>2</sub> with the breakthrough time for SO<sub>2</sub> of 190 and 230 min g<sup>-1</sup>, respectively (Figure 3g,h). The dynamic selectivities of SO<sub>2</sub>/CO<sub>2</sub> are estimated to be 5.2 and 2.5 for MFM-190(F) and MFM-101, respectively (Table S3). This result further confirms the ability of MFM-190(F) and MFM-101 to selectively capture SO<sub>2</sub> with an efficiency down to <0.1 ppm from 2500 ppm in a single adsorption cycle under dry conditions. Furthermore, the excellent stability of MFM-190(F) has been demonstrated by three cycles of breakthrough separations of SO<sub>2</sub>/N<sub>2</sub> (2500 ppm SO<sub>2</sub>) (Figure S20).

The performance of the state-of-the-art porous materials for SO<sub>2</sub> adsorption under ambient conditions is summarized in Table S3 and Figure 3i. Of the MOFs with *nbo* topology, MFM-101 and MFM-190(F) exhibit the most promising stability and uptake capacity, comparable to those of MIL-101(Cr)-4F(1%), which is the previous record holder for SO<sub>2</sub> adsorption at 298 K and 1 bar for a porous material that is stable to repeated SO<sub>2</sub> cycling.<sup>32</sup> Unlike MIL-101(Cr)-4F(1%), which does not show saturation at 1 bar, the isotherms for MFM-190(F) and MFM-101 both exhibit a reversible type I profile. MIL-101(Cr)-4F(1%) exhibits apparent hysteresis of up to 2 mmol g<sup>-1</sup> during desorption at 298 K below 800 mbar, attributed to the relatively strong SO<sub>2</sub>-framework interaction, as evidenced by the calculated heat of adsorption ( $Q_{st}$ ) of 54.3 kJ mol<sup>-1</sup>.<sup>32</sup> In MFM-190(F) and MFM-101, hysteresis during desorption is less dramatic and begins around 200 mbar. The value of  $Q_{st}$  for both MFM-190(F) and MFM-101 is around 35–40 kJ mol<sup>-1</sup> (Figure 3f), notably weaker than that of MIL-101(Cr)-4F(1%), consistent with a narrower hysteresis and a more facile desorption with a lower energy penalty in the former pair of materials. The lack of functional groups in MFM-190(H) results in a lower value for  $Q_{st}$  of 29–41 kJ mol<sup>-1</sup> for SO<sub>2</sub> adsorption. With increasing loading of SO<sub>2</sub>, the MFM-190 materials display a decrease in  $Q_{st}$ , indicating reduced host–guest interactions as the primary binding sites become occupied. MFM-100 and MFM-102 exhibit increases in  $Q_{st}$  upon SO<sub>2</sub> loading, which is likely related perhaps to the partial structural collapse/changes of the framework. The value of  $Q_{st}$  for MFM-101 decreases at low loadings and then increases upon further uptake of SO<sub>2</sub>, consistent with the presence of strong guest–guest interactions in the pore at high surface coverage and the high uptakes and stability. Owing to the absence of open Cu(II) sites, the value

of  $Q_{st}$  for MFM-126 increases steadily with SO<sub>2</sub> loading, reflecting the presence of host–guest interactions throughout the adsorption process.

**Determination of Binding Domains for Adsorbed SO<sub>2</sub>.** The adsorption domains of SO<sub>2</sub> in MFM-190(F) and MFM-126 were determined by *in situ* NPD at 7 K in order to gain insights into the role of open Cu(II) sites and ligand functionalization. Structural analysis of desolvated materials confirms the complete removal of free solvents from the pores and of the coordinated water molecule on the Cu(II) sites of MFM-190, thus creating twelve and six open Cu(II) sites in cages A and B, respectively. Refinement of the NPD data of SO<sub>2</sub>-loaded MOFs revealed significant nuclear density within the pores. These were assigned as four (I–IV) distinct sites for SO<sub>2</sub> in MFM-190(F) [Cu<sub>2</sub>(C<sub>21</sub>H<sub>12</sub>FNO<sub>10</sub>)·(SO<sub>2</sub>)<sub>3.2</sub>] (Figure 4) and one (I') distinct site for SO<sub>2</sub> in MFM-126 [Cu<sub>2</sub>(C<sub>35</sub>H<sub>35</sub>N<sub>9</sub>O<sub>13</sub>)·(SO<sub>2</sub>)<sub>1.6</sub>] (Figure 5).

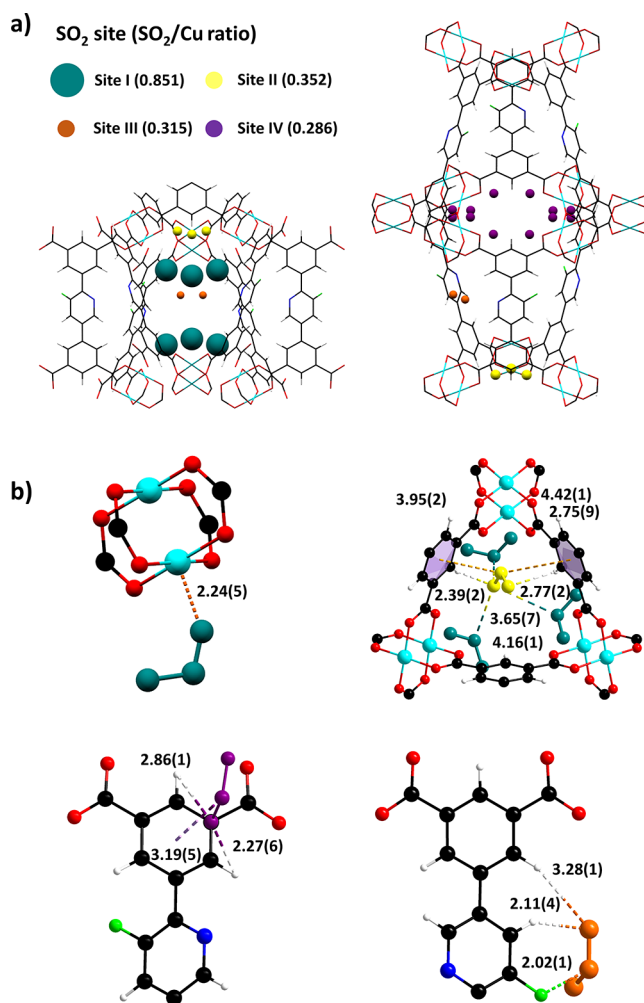


**Figure 4.** Views of the crystal structures of [Cu<sub>2</sub>C<sub>21</sub>H<sub>12</sub>FNO<sub>10</sub>·(SO<sub>2</sub>)<sub>3.6</sub>] derived from the NPD experiments. (a) Binding domains for SO<sub>2</sub> in the cylindrical cage A and the spherical cage B of MFM-190(F). SO<sub>2</sub> molecules are represented by a single sphere at the S positions and are scaled according to their occupancies (Site I: turquoise, Site II: yellow, Site III: pink, and Site IV: orange). (b) Views of binding sites for SO<sub>2</sub> in MFM-190(F) (Site I: turquoise, Site II: yellow, Site III: magenta, and Site IV: orange). (The interatomic distances are in angstrom. Cu, cyan; C, black; O, red; H, white; N, blue; F, green).

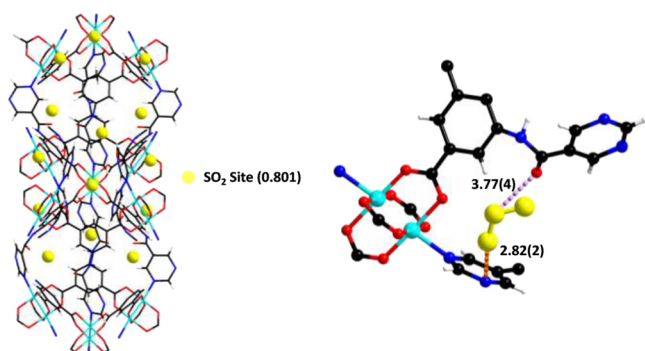


**Figure 5.** Views of the structures of  $[\text{Cu}_2\text{C}_{35}\text{H}_{35}\text{N}_9\text{O}_{13}(\text{SO}_2)_{1.6}]$  derived from the NPD experiment and of the primary binding site of  $\text{SO}_2$  in MFM-126.  $\text{SO}_2$  molecules are represented by a single sphere at the S positions (left) with a detailed view of the primary binding site (right). The interatomic distances are in angstrom. Cu, cyan; C, black; O, red; H, white; N, blue;  $\text{SO}_2$ , yellow.

In  $\text{SO}_2$ -loaded MFM-190(F), the primary binding site, Site I ( $\text{SO}_2/\text{Cu} = 0.785$ ), is located in the spherical cage B, with  $\text{SO}_2$  interacting end-on to the open Cu(II) site [ $\text{O}_{\text{SO}_2}\text{--Cu} = 2.24(5)$  Å,  $\angle\text{S--O--Cu} = 146^\circ$ ] (Figure 4). Site II ( $\text{SO}_2/\text{Cu} = 0.296$ ) sits approximately co-planar with the three  $[\text{Cu}_2(\text{OOCR})_4]$  paddlewheels that define the boundary of the cylindrical and spherical cages, sandwiched between three phenyl rings that link the paddlewheels together. The  $\text{SO}_2$  molecule is located closer to one of the  $[\text{Cu}_2(\text{OOCR})_4]$  paddlewheels than the other two, with a potential side-on interaction between the delocalized  $\pi$  systems of the two neighboring phenyl rings and  $\text{S}_{\text{SO}_2}$  [ $\delta+$ ,  $\text{S}_{\text{SO}_2}\cdots\pi_{\text{left}} = 3.95(2)$  Å,  $\text{S}_{\text{SO}_2}\cdots\pi_{\text{right}} = 4.42(1)$  Å]. Site II is further stabilized *via* two-fold hydrogen bonding between  $\text{O}_{\text{SO}_2}$  and the hydrogen atom on the phenyl ring [ $\text{O}_{\text{SO}_2}\cdots\text{H--R} = 2.39(2)$  and  $2.77(2)$  Å,  $\angle\text{O}\cdots\text{H--C} = 148$  and  $134^\circ$ ]. In addition, the dipole–dipole interactions [ $\text{O}_{\text{SO}_2}\cdots\text{S}_{\text{SO}_2} = 2.76(1)$ ,  $3.65(7)$ , and  $4.16(1)$  Å] between  $\text{SO}_2$  molecules at Sites I and II further stabilize the packing of  $\text{SO}_2$ . Interestingly, the primary and secondary sites for  $\text{SO}_2$  are opposite to those found in  $\text{SO}_2$ -loaded MFM-170,<sup>31</sup> where the open Cu(II) sites serve as secondary binding sites. One possible explanation for this is that half of the axial positions in MFM-170 are blocked by a pyridyl N-center from the linker, and some steric hindrance may be present around the open Cu(II) site. By contrast, all Cu(II) sites in MFM-190(F) can bind  $\text{SO}_2$ , coupled with the presence of additional  $-\text{F}$  sites, contributing to the enhanced uptake of  $\text{SO}_2$ .

Site III ( $\text{SO}_2/\text{Cu} = 0.287$ ) is found at the center of the cylindrical cage, located near the six terminal phenyl rings that connect the central three  $[\text{Cu}_2(\text{OOCR})_4]$  paddlewheels. The  $\text{SO}_2$  molecule is offset to the phenyl ring and stabilized by dipole–dipole interactions between the delocalized  $\pi$  system and  $\text{S}_{\text{SO}_2}$  [ $\text{O}_{\text{SO}_2}\cdots\pi$  system =  $3.19(5)$  Å] and electrostatic interactions between H from the phenyl rings and the O-center from the  $\text{SO}_2$  [ $\text{R--H}\cdots\text{O}_{\text{SO}_2} = 2.27(6)$  and  $2.86(1)$  Å]. Site IV ( $\text{SO}_2/\text{Cu} = 0.232$ ) lies in the window between the cylindrical and spherical cages, sandwiched between two Lewis basic pyridyl rings. Interestingly, similar to that observed in SIFSIX,<sup>28</sup> this binding site is stabilized by a side-on  $\text{S}^{\delta+}\cdots\text{F}^{\delta-}$  electrostatic interaction [ $\text{S}\cdots\text{F} = 2.02(1)$  Å], coupled with two-fold hydrogen bonds between the  $\text{O}_{\text{SO}_2}$  and the hydrogen atom

on the phenyl ring [ $\text{O}_{\text{SO}_2}\cdots\text{H--R} = 2.11(4)$  and  $3.28(1)$  Å,  $\angle\text{O}\cdots\text{H--C} = 143$  and  $139^\circ$ ]. This result confirms that beyond acting as an active site for  $\text{SO}_2$  binding, the primary role of the  $-\text{F}$  group is to increase the framework stability toward  $\text{SO}_2$  adsorption, consistent with the notable difference in the adsorption stability between MFM-190(F) and MFM-190(H).

A very small amount of  $\text{SO}_2$  was loaded into desolvated MFM-126 in order to probe the primary binding site in the absence of an open Cu(II) site. As a result, only one binding site (I') for  $\text{SO}_2$  with a  $\text{SO}_2/\text{Cu}$  ratio of 0.801 is observed and is located in the window between the larger cylindrical cage and the smaller spherical cage, similar to Site IV in MFM-190(F) (Figure 5). Site I' in MFM-126 is stabilized *via* dipole–dipole interactions between  $\text{S}_{\text{SO}_2}$  and the oxygen of the amide group [ $\text{S}_{\text{SO}_2}\cdots\text{O}=\text{C} = 3.77(4)$  Å] as well as between  $\text{O}_{\text{SO}_2}$  and the nitrogen atom of the pyridine ring [ $\text{O}_{\text{SO}_2}\cdots\text{N--R} = 2.82(2)$  Å]. Both of these interactions appear to be weaker than those in Site IV of MFM-190(F), consistent with its low adsorption uptake.

Overall, the end-on binding interaction between  $\text{SO}_2$  and the open Cu(II) sites located at the axial positions of the  $[\text{Cu}_2(\text{OOCR})_4]$  paddlewheels play a significant role in the high  $\text{SO}_2$  capacity of MFM-190(F), displaying the highest  $\text{SO}_2/\text{Cu}$  ratio and the strongest host–guest interaction. In contrast, the primary binding site in MFM-126 is only weakly stabilized. Thus, the *in situ* NPD study has directly rationalized the adsorption performance of these materials.

**In Situ Spectroscopic Analysis of Host–Guest Binding Dynamics.** The binding dynamics of MFM-190(F), MFM-126, MFM-190(H), and MFM-101 upon adsorption of  $\text{SO}_2$  have been analyzed using *in situ* synchrotron infrared microspectroscopy (Figure 6). Desolvated MFM-190(F) shows a number of characteristic peaks at 1556, 1149, 919, and 896  $\text{cm}^{-1}$  (denoted as I, II, III, and IV) (Figure 6a). Peak I is assigned to the distortion of the phenyl ring and Peaks II and III to the in-plane and out-of-plane bending modes of the aromatic C–H groups, respectively.<sup>38</sup> Peak IV is assigned to the C–F stretching.<sup>39</sup> On dosing with  $\text{SO}_2$  (0–1 bar), a blue shift of 6  $\text{cm}^{-1}$  is observed for Peak I to 1562  $\text{cm}^{-1}$ , indicating a stiffening effect of the  $\pi$  system upon binding of  $\text{SO}_2$  molecules to the phenyl ring (Figure 6a). The red shift ( $\Delta = 4$   $\text{cm}^{-1}$ ) of Peak II reflects the presence of  $-\text{CH}^{\delta+}\cdots\delta^-\text{OSO}$  supramolecular contacts (Figure 6b). Furthermore, blue shifts of Peaks III and IV to 926 and 900  $\text{cm}^{-1}$  ( $\Delta = 7$  and  $4$   $\text{cm}^{-1}$ , respectively) are observed, consistent with the presence of hydrogen bonds and dipole–dipole interaction as observed in crystallographic studies (Figure 6c).

Two characteristic peaks at 1639 and 1602  $\text{cm}^{-1}$  are observed for desolvated MFM-126 (Figure 6d), which are assigned to the stretching modes of the C=O group and pyrimidine ring, respectively.<sup>38</sup> Red shifts to 1632 and 1594  $\text{cm}^{-1}$  ( $\Delta = 7$  and  $8$   $\text{cm}^{-1}$ , respectively) upon binding of  $\text{SO}_2$  suggest dipole–dipole interactions with C=O and C=N bonds, again consistent with the crystallographic model.

Desolvated MFM-190(H) (Figures S28–S32) shows a number of characteristic peaks at 1712, 1218, 1027, 838, and 680  $\text{cm}^{-1}$  (denoted as I, II, III, IV, and V). Peak I is assigned to the stretching of the C=O bond and Peaks II and III to the symmetric and asymmetric stretching modes of the C–O bond, respectively. Peaks IV and V are assigned to the in-plane and out-of-plane bending modes of the C–H group of the aromatic ring, respectively. Notable shifts are observed upon

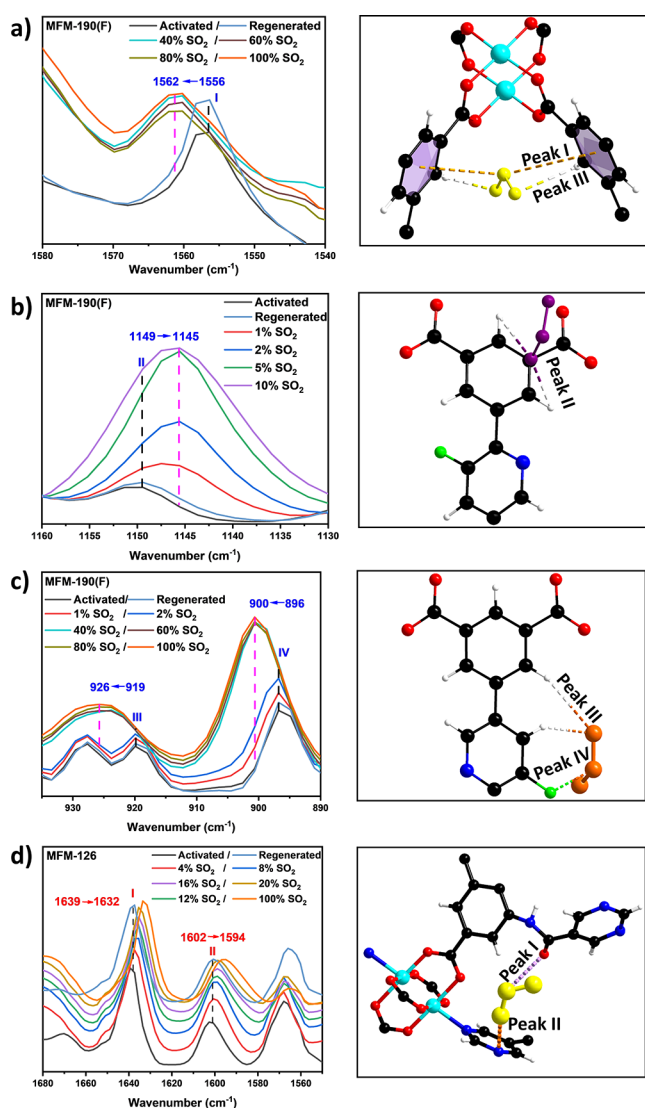


**Figure 6.** *In situ* synchrotron FTIR microspectra of selected MOFs as a function of SO<sub>2</sub> adsorption (left) and views of the corresponding structural model (right). (a) Interaction with phenyl rings in MFM-190(F) at various loadings of SO<sub>2</sub>. (b) C–H in-plane mode in MFM-190(F) at various loadings of SO<sub>2</sub>. Data at high loading are omitted for clarity. (c) C–H out-of-plane mode and C–F stretching in MFM-190(F) at various loadings of SO<sub>2</sub>. (d) Stretching modes of C=O and C=N groups in MFM-126 at various loadings of SO<sub>2</sub>.

SO<sub>2</sub> dosing for Peak I (from 1712 to 1697 cm<sup>-1</sup>), Peak II (from 1218 to 1228 cm<sup>-1</sup>), and Peak III (from 1027 to 1022 cm<sup>-1</sup>), indicating interactions between adsorbed SO<sub>2</sub> molecules and the carboxylate group.<sup>38,40</sup> The blue shifts at Peak IV (from 838 to 850 cm<sup>-1</sup>) and Peak IV (from 680 to 686 cm<sup>-1</sup>) suggest the presence of hydrogen bonds between the aromatic C–H groups and adsorbed SO<sub>2</sub> molecules.

Upon adsorption of SO<sub>2</sub> in MFM-101, four bands experience an obvious shift (Figures S33–S35). The red shift at Peak I from 1637 to 1631 cm<sup>-1</sup> suggests distortion of the phenyl ring due upon binding of SO<sub>2</sub>.<sup>38,40</sup> The shift of Peak II from 1299 to 1311 cm<sup>-1</sup> is consistent with the formation of supramolecular interactions between SO<sub>2</sub> and the C–O group. The blue shifts of Peak III (from 838 to 844 cm<sup>-1</sup>) and Peak IV (from 769 to 773 cm<sup>-1</sup>) confirm the formation of host–guest hydrogen bonds with aromatic C–H groups. All changes

are reversible upon regeneration under a flow of dry N<sub>2</sub>, consistent with the excellent reversibility and stability of SO<sub>2</sub> adsorption in MFM-101.

## CONCLUSIONS

Remarkable and reversible adsorption of SO<sub>2</sub> has been achieved by MFM-101 and MFM-190(F), 18.7 and 18.3 mmol g<sup>-1</sup> at 298 K and 1 bar, respectively. Importantly, MFM-101 shows the highest reversible SO<sub>2</sub> adsorption in porous solids to date. Additionally, MFM-101 and MFM-190(F) both show excellent stability toward multiple cycles of adsorption–desorption of SO<sub>2</sub>. The introduction of a –F group in MFM-190(F) significantly improves the stability and efficacy of the resultant framework upon SO<sub>2</sub> adsorption compared with the non-functionalized MFM-190(H) as well as delivering additional binding sites. Open Cu(II) sites in MFM-190(F) were identified as the strongest adsorption sites for SO<sub>2</sub> by Rietveld refinements of the *in situ* NPD data. Another MOF with exceptional stability toward SO<sub>2</sub> is MFM-126, which has no open metal sites, although this results in a much lower observed capacity toward SO<sub>2</sub> (7.3 mmol g<sup>-1</sup> at 298 K and 1 bar) compared with MFM-190(F) and MFM-101. The dynamics involved in the binding of SO<sub>2</sub> in MFM-126, MFM-190(F), MFM-101, and MFM-190(H) have been investigated by *in situ* spectroscopic techniques, further confirming the formation of supramolecular interactions with SO<sub>2</sub>. Studies of MFM-100, MFM-101, and MFM-102 suggest that a simple increase in surface area is not necessarily linked to the enhanced adsorption of SO<sub>2</sub>, in sharp contrast to the observation of their performance in H<sub>2</sub> adsorption.<sup>35</sup> These studies suggest that the collective contributions from open metal sites, ligand functionalization, and pore geometry have resulted in high and reversible adsorption of SO<sub>2</sub> in these Cu(II)-carboxylate-based MOF materials.

## ASSOCIATED CONTENT

### Supporting Information

The Supporting Information is available free of charge at <https://pubs.acs.org/doi/10.1021/jacs.2c03280>.

Detailed synthesis, characterization and analysis of the crystal structures of all MOFs, TGA, porosity and heat of adsorption measurements, breakthrough experiments, FT-IR microspectroscopy, and Rietveld refinements of neutron diffraction data (PDF)

## Accession Codes

CCDC 1863378–1863380 and 2142215–2142216 contain the supplementary crystallographic data for this paper. These data can be obtained free of charge via [www.ccdc.cam.ac.uk/data\\_request/cif](http://www.ccdc.cam.ac.uk/data_request/cif), or by emailing [data\\_request@ccdc.cam.ac.uk](mailto:data_request@ccdc.cam.ac.uk), or by contacting The Cambridge Crystallographic Data Centre, 12 Union Road, Cambridge CB2 1EZ, UK; fax: +44 1223 336033.

## AUTHOR INFORMATION

### Corresponding Authors

Martin Schröder – Department of Chemistry, University of Manchester, Manchester M13 9PL, U.K.; [orcid.org/0000-0001-6992-0700](https://orcid.org/0000-0001-6992-0700); Email: [M.Schroder@manchester.ac.uk](mailto:M.Schroder@manchester.ac.uk)

Sihai Yang – Department of Chemistry, University of Manchester, Manchester M13 9PL, U.K.; [orcid.org/0000-0002-1111-9272](https://orcid.org/0000-0002-1111-9272); Email: [Sihai.Yang@manchester.ac.uk](mailto:Sihai.Yang@manchester.ac.uk)

## Authors

- Weiyao Li – Department of Chemistry, University of Manchester, Manchester M13 9PL, U.K.
- Jiangnan Li – Department of Chemistry, University of Manchester, Manchester M13 9PL, U.K.
- Thien D. Duong – Department of Chemistry, University of Manchester, Manchester M13 9PL, U.K.
- Sergei A. Sapchenko – Department of Chemistry, University of Manchester, Manchester M13 9PL, U.K.; [orcid.org/0000-0002-2567-1594](https://orcid.org/0000-0002-2567-1594)
- Xue Han – Department of Chemistry, University of Manchester, Manchester M13 9PL, U.K.
- Jack D. Humby – Department of Chemistry, University of Manchester, Manchester M13 9PL, U.K.
- George F. S. Whitehead – Department of Chemistry, University of Manchester, Manchester M13 9PL, U.K.; [orcid.org/0000-0003-1949-4250](https://orcid.org/0000-0003-1949-4250)
- Iñigo J. Victórica-Yrezábal – Department of Chemistry, University of Manchester, Manchester M13 9PL, U.K.
- Ivan da Silva – ISIS Facility, STFC Rutherford Appleton Laboratory, Chilton, Oxfordshire OX11 0QX, U.K.; [orcid.org/0000-0002-4472-9675](https://orcid.org/0000-0002-4472-9675)
- Pascal Manuel – ISIS Facility, STFC Rutherford Appleton Laboratory, Chilton, Oxfordshire OX11 0QX, U.K.
- Mark D. Frogley – Diamond Light Source, Harwell Science and Innovation Campus, Oxfordshire OX11 0DE, U.K.
- Gianfelice Cinque – Diamond Light Source, Harwell Science and Innovation Campus, Oxfordshire OX11 0DE, U.K.; [orcid.org/0000-0001-6801-8010](https://orcid.org/0000-0001-6801-8010)

Complete contact information is available at:  
<https://pubs.acs.org/10.1021/jacs.2c03280>

## Author Contributions

<sup>#</sup>W.L., J.L., and T.D.D. contributed equally to this work.

## Notes

The authors declare no competing financial interest.

## ACKNOWLEDGMENTS

We thank EPSRC (EP/I011870, EP/P001386), The Royal Society, and The University of Manchester for funding. This project has received funding from the European Research Council (ERC) under the European Union's Horizon 2020 Research and Innovation Programme (grant agreement No 742401, NANOCHEM). We are grateful to STFC/ISIS facility for access to Beamlines TOSCA and WISH, and we thank Mark Kibble and other beamline support staff for their help during beam time. We thank Diamond Light Source for access to Beamlines I19 and B22.

## REFERENCES

- (1) U.S. Energy Information Administration. *International Energy Outlook*; U.S. Energy Information Administration: Washington, DC, 2019.
- (2) Clean Air for a Sustainable World. *Nat. Commun.* **2021**, *12*, 5824.
- (3) Ou, Y.; West, J.; Smith, S.; Nolte, C.; Loughlin, D. Air Pollution Control Strategies Directly Limiting Nation Health Damages in the US. *Nat. Commun.* **2020**, *11*, 957.
- (4) Vanduyck, T.; Keramidis, K.; Kitous, A.; Spadaro, J.; Dingenen, R.; Holland, M.; Saveyn, B. Air Quality Co-benefits for Human Health and Agriculture Counterbalance Costs to Meet Paris Agreement Pledges. *Nat. Commun.* **2018**, *9*, 4939.
- (5) Zhang, L.; Liu, W.; Hou, K.; Lin, J.; Song, C.; Zhou, C.; Huang, B.; Tong, X.; Wang, J.; Rhine, W.; Jiao, Y.; Wang, Z.; Ni, R.; Liu, M.; Zhang, L.; Wang, Z.; Wang, Y.; Li, X.; Liu, S.; Wang, Y. Air Pollution Exposure Associates with Increased Risk of Neonatal Jaundice. *Nat. Commun.* **2019**, *10*, 3741.
- (6) Sulfur Dioxide. *Ullmann's Encyclopedia of Industrial Chemistry*. Wiley-VCH, 2003.
- (7) Srivastava, R. K.; Jozewicz, W.; Singer, C. SO<sub>2</sub> Scrubbing Technologies: a Review. *Environ. Prog.* **2001**, *20*, 219–228.
- (8) Mathieu, Y.; Tzanis, L.; Soulard, M.; Patarin, J.; Vierling, M.; Moliere, M. Adsorption of SO<sub>x</sub> by Oxide Materials: a Review. *Fuel Process. Technol.* **2013**, *114*, 81–100.
- (9) Bandosz, T. *Activated Carbon Surfaces in Environmental Remediation*; Elsevier, 2006; pp. 231–292, DOI: [10.1016/S1573-4285\(06\)80014-1](https://doi.org/10.1016/S1573-4285(06)80014-1).
- (10) Srinivasan, A.; Grutzeck, M. The Adsorption of SO<sub>2</sub> by Zeolites Synthesized from Fly Ash. *Environ. Sci. Technol.* **1999**, *33*, 1464–1469.
- (11) Ivanova, E.; Koumanova, B. Adsorption of Sulfur Dioxide on Natural Clinoptilolite Chemically Modified with Salt Solutions. *J. Hazard. Mater.* **2009**, *167*, 306–312.
- (12) Woellner, M.; Hausdorf, S.; Klein, N.; Mueller, P.; Smith, M.; Kaskel, S. Adsorption and Detection of Hazardous Trace Gases by Metal–organic Frameworks. *Adv. Mater.* **2018**, *30*, 1–27.
- (13) Liang, Z.; Qu, C.; Guo, W.; Zou, R.; Xu, Q. Pristine Metal–organic Frameworks and Their Composites for Energy Storage and Conversion. *Adv. Mater.* **2018**, *30*, 1702891.
- (14) Banerjee, R.; Furukawa, H.; Britt, D.; Knobler, C.; O'Keeffe, M.; Yaghi, O. Control of Pore Size and Functionality in Isoreticular Zeolitic Imidazolate Frameworks and Their Carbon Dioxide Selective Capture Properties. *J. Am. Chem. Soc.* **2009**, *131*, 3875–3877.
- (15) Chen, B.; Eddaoudi, M.; Reineke, T.; Kampf, J.; O'Keeffe, M.; Yaghi, O. Cu<sub>2</sub>(ATC)·6H<sub>2</sub>O: Design of Open Metal Sites in Porous Metal–organic Crystals (ATC: 1, 3, 5, 7-Adamantane Tetracarboxylate). *J. Am. Chem. Soc.* **2000**, *122*, 11559–11560.
- (16) He, C.; Hou, C.; Wang, Y.; Gong, X.; Jiang, H.; Sun, Y.; Liu, K.; Cao, X. Open Metal Site (OMS) and Lewis Basic Site (LBS)-Functionalized Copper–organic Framework with High CO<sub>2</sub> Uptake Performance and Highly Selective CO<sub>2</sub>/N<sub>2</sub> and CO<sub>2</sub>/CH<sub>4</sub> Separation. *CrystEngComm* **2020**, *22*, 3378–3384.
- (17) Lin, R.; Xiang, S.; Zhou, W.; Chen, B. Microporous Metal–organic Framework Materials for Gas Separation. *Chem* **2020**, *6*, 337–363.
- (18) Bloch, E.; Queen, W.; Krishna, R.; Zadrozny, J.; Brown, C.; Long, J. Hydrocarbon Separations in a Metal–organic Framework with Open Iron(II) Coordination Sites. *Science* **2012**, *335*, 1606–1610.
- (19) Han, X.; Yang, S.; Schröder, M. Porous Metal–organic Frameworks as Emerging Sorbents for Clean Air. *Nat. Rev. Chem.* **2019**, *3*, 108–118.
- (20) (a) Martinez-Ahumada, E.; Lopez-Olvera, A.; Jancik, V.; Sanchea-Bautista, J.; Gonzalez-Zamora, E.; Martis, V.; Williams, D.; Ibarra, I. MOF Materials for the Capture of Highly Toxic H<sub>2</sub>S and SO<sub>2</sub>. *Organometallics* **2020**, *39*, 883–915. (b) Suo, X.; Yu, Y.; Qian, S.; Zhou, L.; Cui, X.; Xing, H. Tailoring the pore size and chemistry of ionic ultramicroporous polymers for trace sulfur dioxide capture with high capacity and selectivity. *Angew. Chem., Int. Ed.* **2021**, *60*, 6986–6991.
- (21) Chen, R.; Zhang, T.; Guo, Y.; Wang, J.; Wei, J.; Yu, Q. Recent Advances in Simultaneous Removal of SO<sub>2</sub> and NO<sub>x</sub> from Exhaust Gases: Removal Process, Mechanism and Kinetics. *Chem. Eng. J.* **2021**, *420*, No. 127588.
- (22) (a) Brandt, P.; Nuhnen, A.; Lange, M.; Möllmer, J.; Weingart, O.; Janiak, C. Metal–organic Frameworks with Potential Application for SO<sub>2</sub> Separation and Flue Gas Desulfurization. *ACS Appl. Mater. Interfaces* **2019**, *11*, 17350–17358. (b) Brandt, P.; Xing, S. H.; Liang, J.; Kurt, G.; Nuhnen, A.; Weingart, O.; Janiak, C. Zirconium and Aluminum MOFs for Low-Pressure SO<sub>2</sub> Adsorption and Potential Separation: Elucidating the Effect of Small Pores and NH<sub>2</sub> Groups. *ACS Appl. Mater. Interfaces* **2021**, *13*, 29137–29149.

- (23) Savage, M.; Cheng, Y.; Easun, T.; Eyley, J.; Argent, S.; Warren, M.; Lewis, W.; Murray, C.; Tang, C.; Frogley, M.; Cinque, G.; Sun, J.; Rudić, S.; Murden, R.; Benham, M.; Fitch, A.; Blake, A.; Ramirez-Cuesta, A.; Yang, S.; Schröder, M. Selective Adsorption of Sulfur Dioxide in a Robust Metal–organic Framework Material. *Adv. Mater.* **2016**, *28*, 8705–8711.
- (24) Zárate, J.; Sánchez-González, E.; Williams, D.; González-Zamora, E.; Martis, V.; Martínez, A.; Balmaseda, J.; Maurin, G.; Ibarra, I. High and Energy-efficient Reversible SO<sub>2</sub> Uptake by a Robust Sc(III)-Based MOF. *J. Mater. Chem. A* **2019**, *7*, 15580–15584.
- (25) Xing, S.; Liang, J.; Brandt, P.; Schäfer, F.; Nuhnen, T.; Boldog, I.; Mölmer, J.; Lange, M.; Weingart, O.; Janiak, C. Capture and Separation of SO<sub>2</sub> Traces in Metal–Organic Frameworks via Pre-synthetic Pore Environment Tailoring by Methyl Groups. *Angew. Chem., Int. Ed.* **2021**, *60*, 17998–18005.
- (26) Gorla, S.; Diaz-Ramirez, M.; Abeynayake, N.; Kaphan, D.; Williams, D.; Martis, V.; Lara-Garcia, H.; Donnadiou, B.; Lopez, N.; Ibarra, I.; Montiel-Palma, V. Functionalized NU-1000 with an Iridium Organometallic Fragment: SO<sub>2</sub> Capture Enhancement. *ACS Appl. Mater. Interfaces* **2020**, *12*, 41758–41764.
- (27) Cui, X.; Yang, Q.; Yang, L.; Krishna, R.; Zhang, Z.; Bao, Z.; Wu, H.; Ren, Q.; Zhou, W.; Chen, B.; Xing, H. Ultrahigh and Selective SO<sub>2</sub> Uptake in Inorganic Anion-pillared Hybrid Porous Materials. *Adv. Mater.* **2017**, *29*, 1606929.
- (28) Gong, W.; Xie, Y.; Pham, T.; Shetty, S.; Son, F.; Idrees, K.; Chen, Z.; Xie, H.; Liu, Y.; Snurr, R.; Chen, B.; Alameddine, B.; Cui, Y.; Farha, O. Creating Optimal Pockets in a Clathrocholate-based Metal–organic Framework for Gas Adsorption and Separation: Experimental and Computational Studies. *J. Am. Chem. Soc.* **2022**, *144*, 3737–3745.
- (29) Carter, J.; Han, X.; Moreau, F.; da Silva, I.; Nevin, A.; Godfrey, H.; Tang, C.; Yang, S.; Schröder, M. Exceptional Adsorption and Binding of Sulfur Dioxide in a Robust Zirconium-based Metal–organic Framework. *J. Am. Chem. Soc.* **2018**, *140*, 15564–15567.
- (30) Zhang, Z.; Yang, B.; Wu, Y.; Zhang, W.; Ma, Y. Post Modification of Oxo-cluster in Robust Zirconium-based Metal Organic Framework for Durable SO<sub>2</sub> Capture from Flue Gas. *Sep. Purif. Technol.* **2021**, *276*, No. 119349.
- (31) Smith, G.; Eyley, J.; Han, X.; Zhang, X.; Li, J.; Jacques, N.; Godfrey, H.; Argent, S.; McCormick McPherson, L.; Teat, S.; Cheng, Y.; Frogley, M.; Cinque, G.; Day, S.; Tang, C.; Easun, T.; Rudić, S.; Ramirez-Cuesta, A.; Yang, S.; Schröder, M. Reversible Coordinative Binding and Separation of Sulfur Dioxide in a Robust Metal–organic Framework with Open Copper Sites. *Nat. Mater.* **2019**, *18*, 1358–1365.
- (32) Martínez-Ahumada, E.; Díaz-Ramírez, M.; Lara-García, H.; Williams, D.; Martis, V.; Jancik, V.; Lima, E.; Ibarra, I. High and Reversible SO<sub>2</sub> Capture by a Chemically Stable Cr(III)-Based MOF. *J. Mater. Chem. A* **2020**, *8*, 11515–11520.
- (33) Cambridge Crystallographic Data Centre (CCDC) - MOF subset count (Version 5.38 of the CSD, accessed August 2021).
- (34) Rao, X.; Cai, J.; Yu, J.; He, Y.; Wu, C.; Zhou, W.; Yildirim, T.; Chen, B.; Qian, G. A Microporous Metal–organic Framework with both Open Metal and Lewis Basic Pyridyl Sites for High C<sub>2</sub>H<sub>2</sub> and CH<sub>4</sub> Storage at Room Temperature. *Chem. Commun.* **2013**, *49*, 6719–6721.
- (35) Lin, X.; Telepeni, I.; Blake, A.; Dailly, A.; Brown, C.; Simmons, J.; Zoppi, M.; Walker, G.; Thomas, K.; Mays, T.; Hubberstey, P.; Champness, N.; Schröder, M. High Capacity Hydrogen Adsorption in Cu(II) Tetracarboxylate Framework Materials: The Role of Pore Size, Ligand Functionalization, and Exposed Metal Sites. *J. Am. Chem. Soc.* **2009**, *131*, 2159–2171.
- (36) Humby, J.; Benson, O.; Smith, G.; Argent, S.; da Silva, I.; Cheng, Y.; Rudić, S.; Manuel, P.; Frogley, M.; Cinque, G.; Saunders, L.; Vitórica-Yrezábal, I.; Whitehead, G.; Easun, T.; Lewis, W.; Blake, A.; Ramirez-Cuesta, A.; Yang, S.; Schröder, M. Host–guest Selectivity in a Series of Isorecticular Metal–organic Frameworks: Observation of Acetylene-to-Alkyne and Carbon Dioxide-to-Amide Interactions. *Chem. Sci.* **2019**, *10*, 1098–1106.
- (37) Yang, S.; Liu, L.; Sun, J.; Thomas, K.; Davies, A.; George, M.; Blake, A.; Hill, A.; Fitch, A.; Tang, C.; Schröder, M. Irreversible Network Transformation in a Dynamic Porous Host Catalyzed by Sulfur Dioxide. *J. Am. Chem. Soc.* **2013**, *135*, 4954–4957.
- (38) *Infrared Spectroscopy Absorption Table* <https://chem.libretexts.org/@go/page/22645>.
- (39) Ramasamy, R. FTIR and FT-RAMAN Spectral Investigation of Fluorobenzene. *Int. J. Phys. Appl.* **2014**, *6*, 1–6.
- (40) Smith, B. The C=O Bond, Part VI: Ester and the Rule of Three. *Spectroscopy* **2018**, *22*, 20–23.